Supporting Information

Ludington et al. 10.1073/pnas.1217354110

SI Materials and Methods

Strains and Cell Culture. Results reported in the main text were derived from a kinesin-associated protein on the heterotrimeric kinesin-2 complex (KAP)-green fluorescent protein (GFP) rescue of the flagellar assembly mutant-3 (fla3) mutant, generously provided by Mary Porter (University of Minnesota, Minneapolis) (1). A backcross to CC125 (*Chlamydomonas* Stock Center) showed no strain-dependent effects and an *lf4*/KAP-GFP/*fla3* strain was produced by mating and PCR-based genotyping. The *lf4* strain used was allele *lf4*-V86, a generous gift from the Dieckmann laboratory (University of Arizona, Tucson, AZ). The strain was verified by genomic PCR, and absences were found in the 5′ region and throughout the coding region.

An intraflagellar transport IFT20-GFP rescue of the null IFT20 mutant was described in ref. 2. The IFT20 strain showed a similar injection trend for injection magnitude vs. time preceding and time following an injection as was seen with KAP-GFP (Fig. S2), but the strain showed a less steep variation in injection rate as a function of flagellar length because the increased intensity of retrograde IFT trains makes background subtraction less precise. Similar features to those of the KAP-GFP strain were observed for bursting and periodicity in this strain (Fig. S2).

All strains were grown on Tris-acetate-phosphate (TAP) agar plates and then transferred to M1 liquid media under continuous light for 12–36 h before fixation or live cell imaging. Lithium chloride (Sigma) was prepared in a 1-M stock in M1 media and used at a 25-mM working concentration in M1. Cells were incubated for 1 h in LiCl before imaging. Cycloheximide (Sigma) was prepared as a 10 mg/mL stock in ethanol and diluted to a 10 μg/mL working concentration. Cells were incubated a minimum of 10 min in cycloheximide before imaging. A 1:1,000 ethanol in M1 media control showed no significant effect on IFT traffic by methods in Fig. 3 (Student's *t* test for distance from the control trend line gave $P > 0.25$).

Fixation. Methanol fixation was performed as previously described (3). In Fig. 4, cells were stained with primary anti-GFP and secondary anti-mouse, labeled with rhodamine. In Fig. S8, cells were incubated with anti-GFP (unlabeled) and imaged in the FITC channel for GFP with no secondary stain. Similar results in the FITC channel were achieved by methanol fixation and overnight incubation in 10% (vol/vol) block with no primary antibody.

Live Cell Deflagellation and Flagellar Regeneration. Cells were deflagellated by passing log-phase culture through an insulin syringe (28 gauge, 1 cc) in M1 culture media. One-half milliliter of culture was first drawn rapidly into the syringe, causing cavitation of the media. The culture was then forced rapidly from the syringe back into a 1.5-mL Eppendorf tube. For long-zero experiments, regeneration proceeded for 15 min in the Eppendorf tube before fixation. For total internal reflection fluorescence (TIRF) microscopy, cells regenerated on the coverslip.

Live Cell Imaging. Live cell imaging was performed on a Nikon te2000 microscope with a 100× 1.49-NA TIRF oil lens and 488-nm laser illumination through an optical fiber with a near-TIRF illumination field. Emitted light from the sample was reflected to the camera, using a 514-nm dichroic mirror and a 525-nm filter. Images were recorded at 29.7 frames per second on a Photometrics QuantEM EMCCD camera with 157 nm per pixel. In a set of experiments to control for effects of the illumination field, an identical microscope setup with a Yokogawa C-22 spinning disk was used. TIRF and spinning-disk confocal imaging gave similar trends for the injection magnitude vs. the time intervals preceding and following an injection, although we did not make a statistical comparison because the two illumination fields produce different injection intensities.

The TIRF field was calibrated for each imaging session by adhering 100-nm orange fluorescent beads (Phosphorex) to a coverslip and then setting the TIRF angle to give a mean bead intensity of 75% the maximum fluorescence intensity detected (minimum 45 beads per view frame). To accomplish this, we imaged the beads over a range of 50 laser angles from below TIR (all light reflected) to above TIR, where all of the light is transmitted. The mean bead intensity was calculated at each angle, using custom MATLAB software. Then, the mean bead intensity vs. laser angle was plotted. The curve shows a characteristic increase up to a maximum and subsequent sharp drop off in intensity as the laser angle increases significantly above TIR. We found empirically that by setting the angle to give a mean bead intensity of 75% the maximum, we could exclude the cell bodies from the illumination field while getting clear illumination of the entire flagellum. Tokunaga et al. (4) describe the technique of near TIR illumination at length. This method produces roughly constant flagellar background intensity over a range of flagellar lengths (Fig. S10*E*).

Cells were allowed to adhere their flagella to the coverglass and then imaged at 29.7 frames per second. The KAP-GFP cells were imaged under two slightly different microscope configurations (RAM in the control computer was increased and the dichroic mirror was replaced). The first set contains 168 control flagella, 18 cycloheximide-treated flagella, and 39 lithium chloride-treated flagella, whereas the second set contains 50 control flagella and 29 *lf4* flagella.

Because the replacement dichroic mirror produces a very slightly higher signal-to-noise ratio, we made an equivalent adjustment in the image-processing background removal and smoothing parameters to allow direct overlay of the two control sets. We compared the two control datasets by the methods in Fig. 3 and found no significant difference—comparing the deviation from the control trend line for injection rate vs. flagellar length, the deviations are not significantly different by two-tailed *t* test ($P = 0.66$). The larger dataset was used for injection magnitude vs. time preceding and following injection plots because more data points are available. The second set was taken with increased RAM. Therefore, this set has longer time series and, accordingly, these results are presented for power spectrum analysis. However, both sets gave equivalent spectra.

IFT Kymograph Analysis. Kymographs were made using hand traces of the flagella in Nikon elements (v3.1) to delineate the initial position of the flagellum. Kymographs were then converted to IFT injection time series, using custom MATLAB software with the algorithm (5) in Fig. 1, using the following specific parameters. We found empirically that the background was best approximated as a constant component plus a photobleaching component. The constant background was estimated as the kymograph minimum and subtracted from the time series (Fig. S10*E*). We then estimated local background as the local time series minimum on a 1.5-s window and then normalized the time series to this local background to account for photobleaching. This step locally detrends the time series and serves as a high-pass filter. The time series were then smoothed using two iterations of a running median filter with a window width of 3 pixels followed by one iteration with a running mean filter of window width 3 pixels.

Injection times were determined automatically as the local maxima in the time series. The minimum size injection that we scored was determined by comparing time series maxima to kymograph traces by eye to determine what intensity could reliably be scored as an injection. From this comparison we set the threshold peak intensity at 0.015 relative intensity units. Injection peak sizes were then calculated as the area under the peak while the time series intensity was greater than 0.68× the local peak maximum. Results were not sensitive to changes in this parameter. Injection sizes were then normalized to the minimum peak size and only injections greater than 10× the minimum injection intensity were counted in the analysis. This step served to remove small peaks in the time series that were due to noise. These methods are described in more detail in ref. 6. We validated the methods and parameter choices by comparing with manual measurements of kymographs that were previously analyzed (6).

We next asked how the observed signal-to-noise ratio affects our analysis. The signal-to-noise ratio was calculated as the square of the ratio of signal amplitude to noise amplitude. Signal amplitude was calculated as the total signal amplitude from the smoothed time series, and noise amplitude was calculated as the total amplitude in the time series after subtracting the smoothed signal amplitude.

For this analysis, we generated synthetic kymograph datasets, using a model convolution approach (7) by resampling the injection series from the real data, convolving the synthetic series by the point-spread function of the microscope, and then adding background and noise to the level measured empirically in the background of real flagella. We then built synthetic datasets over a range of signal-to-noise values representative of the real dataset (Fig. S10). Over the range of measured signal-to-noise values, the highest false positive rate was 6% and the lowest true positive rate was 98%, with a maximum total error of 8%. At the mean signal-to-noise ratio of the dataset, the true positive rate was 100% with 6% false positives. The algorithm tends to have a very high true positive hit rate due in part to the median projection across the kymographs (5).

Taking the median projection greatly reduces the degree to which noise obscures the true signal. Although this method is simple and robust, it does limit the type of kymographs that can be input: There must be a consistent IFT velocity for all trains over the entire flagellum for the entire course of the time series. Therefore, we manually selected time series where the IFT velocity was consistent over the entire kymograph and where minimal background variation was present. We note that the KAP-GFP strain used in this paper produces very faint retrograde IFT traces. Closer inspection of the kymographs and image denoising reveal that there is normal retrograde traffic. The traces are more readily apparent in the IFT20-GFP and other GFP-tagged IFT strains, but the kymograph analysis algorithms perform better on the KAP-GFP kymographs.

In terms of total injected material detected, the algorithm detects 98.4% of the actual input from synthetic data when realistic noise is overlaid on the synthetic kymographs. However, on an injection-by-injection basis, the accuracy is lower, and this inaccuracy increases for larger-magnitude injections (Fig. S10*D*).

Missed observations by this analysis would appear as smaller-magnitude injections for a longer time interval. Undoubtedly, some false negatives occur, but the magnitude vs. preceding time interval plot suggests these are rare (Fig. S7*B*).

For Table S1, to measure the amount of time the injector spends in the open vs. closed state, for each time series we counted the open time as the time for each peak where the intensity remains above 68% of the peak maximum. For bursts, we counted the entire burst duration as open time. We counted the remainder of the time series as closed time. The ratio of open-to-closed time was then calculated for each time series and compared with the injection rate for each time series, using Pearson's correlation coefficient ($r = -0.12$, $P = 0.09$, $n = 218$ flagella).

Relating Intensity Units to the Number of KAP Molecules per Injection Event. As discussed above, the intensity values for the peaks in the time series combine corrections in illumination set by fluorescent bead standards to account for variations in laser power or other aspects of microscopy and normalization of intensity across each kymograph relative to the background intensity to account for photobleaching during data collection. To relate these normalized intensity units to the number of molecules of KAP-GFP in the individual injection events, we compared our results with our previously published results, obtained by stepwise photobleaching on fixed IFT trains (6), which showed that the distribution of KAP-GFP numbers in IFT trains in full-length flagella had an average value of 6 per train and showed a peak in the range of 4–6 KAP-GFP per train. Comparing that result to the distribution of event sizes that we observe, in which the average size of an injection event in full-length wild-type flagella is ~200 (Fig. 3*A*), we find that a single KAP-GFP corresponds to ~33 normalized units.

As a test of this approximate relation between normalized units and KAP-GFP number, we note that previous stepwise photobleaching experiments showed that flagella in the range 0–2 μm contained 16 KAP-GFP per train (6), which would correspond to an expected injection size of ~500 based on our proposed conversion factor. We found that short flagella in this same range had injection sizes with an average magnitude of 463, consistent with the proposed conversion factor.

Burst Integration. Burst integration involves determining at what time resolution the actual events in a time series are occurring. To take the sandpile analogy, we could count individual grains in an avalanche as events, or we could count events as all of the grains that hit the scale within a certain threshold time interval (Fig. 2*A*). For the sandpile, we want to count the avalanches as events, so we integrate grains to get a time series of avalanches. A technical problem occurs when the distribution of intervals between avalanches overlaps with the distribution of intervals between individual grains hitting the scale. This problem is common in ion channel time series, where channel-opening events of two different types overlap in their distributions. An optimal solution, in terms of trade-off between types of errors, is to find a cutoff interval threshold where the events lost from each of the distributions are equal (8). In our data, we determined the threshold time interval of 0.26 s by fitting a sum of two lognormal distributions to the interval time histogram, with the two distributions representing time intervals between bursts (greater mean) and between injections (lower mean). The threshold interval was then set where area in the tail of the within-burst distribution extending above the threshold was equal to the area in the tail of the between-burst distribution extending below the threshold. Injections occurring less than the threshold time apart after the previous injection were then merged into the previous injection. Some time series began or ended in the middle of a burst. These time series were truncated to eliminate the partial bursts.

Power Spectrum Calculation. For power spectrum calculation, we analyzed only time series that had a length of at least 50 s ($n = 37$ time series). For Fig. 1*C* and Fig. S2*A* the power spectrum of background-corrected time series was calculated directly, using Fourier-based methods in MATLAB. For Fig. S3, power and significance were assessed using an adaptation of the algorithm of Ahdesmaki et al. (9).

Because time series smoothing affects the high-frequency part of the power spectrum and background correction affects low frequency, we also calculated the power spectrum of the raw, uncorrected time series (Fig. S11), which shows behavior more typical of a power law.

Analysis of Long-Memory Behavior in IFT Using the Hurst Exponent and the Autocorrelation Function. One hallmark feature seen in many, although not necessary all, avalanche-like systems is long-memory behavior. By convention, a long-memory system is classified as such on the basis of time series analysis of the system behavior. If the time series resembles a random walk, such that changes in the system output are uncorrelated from one time interval to the next, such a system would be considered a short-memory system. If, in contrast, changes in the system are correlated with the state of the system at earlier time points, this would be considered a long-memory system, and the farther back in time the correlation extends, the longer the "memory" of the system.

Analysis of Long-Memory Behavior Using the Hurst Exponent. As stated thus far, "long memory" is not precisely defined. The most standard criterion for long memory, which captures the general spirit of the foregoing conceptual definition, is based on the rate at which the autocorrelation decays over time. If the autocorrelation decays more slowly than a one-dimensional random walk (i.e., Brownian motion), the system is classified as long memory. Although this criterion is expressed in terms of the autocorrelation, to deal with finite record lengths and other pragmatic issues, a more robust estimator known as the Hurst exponent is usually used to test for long-memory behavior. The Hurst exponent is calculated from the time series data (10) and yields a value between 0 and 1. A Hurst exponent of 0.5 indicates a random walk, whereas Hurst exponents greater than 0.5 indicate long-memory behavior. Hurst exponent analysis has been used to demonstrate long-memory behavior in river flows (11), confined plasmas (12, 13), solar activity (14), atmospheric ozone levels (15), and heart-beat fluctuations (16), as well as energy prices (17) and stock market activity (18, 19). Given the preexisting track record for using this criterion in studies of long-memory behavior in such widely varying fields, we used this criterion to assess long memory in IFT time series.

To calculate the Hurst exponent, we considered the time intervals between adjacent injections by converting each injection series into a time series of the time intervals between events. For example, [1.1, 0.9, 1.0, 0.4, 1.2, 0.5] would be a time series of the six intervals between seven injections in the original time series. In this way, we do not consider the event duration in the analysis. To calculate the Hurst exponent (10), we cover the time series with a series of sliding windows of increasing time span τ, and then within each window we generate a mean adjusted series Y from all points in the series within the window, $Y_i = X_{t+i} - \langle X \rangle$ for all times in the window under consideration starting at time t up to $t + \tau$. Next, we calculated the cumulative deviate series $Z_j = \sum_{i=1}^{j} Y_i$ for all times j up to the size τ of the window. We then calculated the range R within each window according to $R = \max(Z_1, Z_2, ..., Z_\tau) - \min(Z_1, Z_2, ..., Z_\tau)$. Next, we computed the SD S of the data points X within each such window. The range R and SD S were then averaged over all windows of duration τ to yield the average range and deviation, $R\tau$ and $S\tau$, for a given time lag t. The rescaled range as a function of time lag is then given by R_τ / S_τ. Finally, we estimated the exponent of the power law fit for the rescaled range as a function of τ. Only time series with more than 10 injections were considered. In the main text we report the Hurst exponent for the time intervals between injections because this value tells us about correlations in injection timing. However, for completeness, we also calculated the exponent for event sizes (mean = 0.64, SEM = 0.031). The value matches with that of the time intervals, which makes intuitive sense because we observe a correlation between injection sizes and time intervals.

Analysis of Long-Memory Behavior Using the Autocorrelation Function. The Hurst exponent thus provides a measure of long-memory behavior without the need to specify a particular timescale of interest. However, in IFT, the time between injections provides a natural timescale that we can use to define what we mean by "long": If correlations between injections exist on a timescale that is significantly longer than the average time between injection events, we can consider such a correlation to be extending over a timescale that is long. This type of analysis has been used, for example, to demonstrate long-memory behavior in human brain activity (20). To apply this method to our data, we analyzed the autocorrelation function of the locally background-subtracted time series data and found that the autocorrelation decays as a double exponential with decay constants of $-1.7\ \mathrm{s}^{-1}$ for the fast component and $-0.0060\ \mathrm{s}^{-1}$ for the slow component. The slow component corresponds to a correlation time of 170 s and appears as a long tail in the autocorrelation. By comparison, the average injection frequencies vary between 0.87 and 1.4 Hz, which corresponds to mean times between events in the range 0.71–1.2 s. The autocorrelation in the IFT time series thus extends two orders of magnitude beyond the timescale defined by the average time between injections, thus supporting the idea that IFT is a long-memory process in this latter sense.

Fixed Cell Imaging and Analysis. ***Fixed cell imaging.*** Fixed samples were imaged on a Deltavision microscope at 100× with filters for FITC and Rhodamine channels. Z-stacks were acquired with a 0.2-μm z-step. Deconvolution was performed using Deltavision software and z-stacks were made for further analysis.

Injector intensity quantification. Custom software was written in MATLAB. Manual segmentation was used to identify cells and IFT injector regions. For each cell, background was subtracted from the z-stack as the mean intensity of the pixels in the 3D bounding box perimeter, and then pixels with intensity greater than one-eighth the maximum intensity were summed to give injector intensity. The one-eighth cutoff was chosen because it consistently produced a good visual overlap with the injector region. Varying the cutoff parameter did not change the overall results. We note that deconvolution is often necessary to distinguish paired basal bodies by epifluorescence.

Intensity ratios in the control, single-cell, and multiple-cell comparison samples (Fig. 4 and Fig. S8) were compared by one-way ANOVA and then multiple pairwise comparisons were made using Bonferroni's correction for α.

Computational Models. Detailed methods with equations are in the Figs. S4 and S6 legends. A one-dimensional agent-based traffic model was formulated on the basis of the molecular motor-based transport model presented in Chowdury et al. (21). Briefly, a linear track of 500 motor-binding positions was established. Motors are then selected at random to step forward one position along the track. Motors that reach the end of the track then enter a pool of motors that can enter the track at position 1. A motor moves only if the position in front of it is unoccupied. Jams develop randomly and jam magnitude is taken to be the number of contiguous motors in a jam after 100,000 time steps.

A one-dimensional Burridge–Knopoff spring-block model for earthquakes (22), formulated on the basis of the Huang and Turcotte (23) three-spring model, was produced with simplified dynamics that would apply at low Reynolds number. Briefly, at each time step, the driving block moves forward by a set amount. The two sliding blocks are coupled to each other and to the driving block by springs. The sliding blocks experience friction with a uniform probability proportional to the length of their surface in contact with the floor. When the spring force exceeds the static frictional force constant on a sliding block, the block moves on the basis of the ratio of forces until the force drops below the sliding friction force constant. The output is the magnitude of the movements of one of the sliding blocks over time. The dynamics are similar to those of the original model when the loading rate is set in the higher range relative to the frictional component.

Statistics. All statistical tests were performed in MATLAB, using the Statistical Analysis Toolbox except where indicated. All correlation values given are the standard Pearson product-moment correlation coefficient (r). P values for correlation are for the test of whether the correlation is nonzero, where $P = 0$ gives 100% certainty of a nonzero correlation.

SI Appendix

Model for IFT Accumulation Based on Ras-related nuclear protein guanosine 5′-triphosphate Gradient-Mediated Length Sensing. Our data show that IFT proteins accumulate at the basal body as a function of flagella length. However, our data do not directly indicate the mechanism by which length may alter IFT accumulation. Dishinger et al. (24) showed that a gradient of Ras-related nuclear protein (Ran) guanosine 5′-triphosphate (GTP) between the ciliary and cytoplasmic compartments regulates entry of proteins into the cilium. We therefore asked whether the RanGTP gradient is, at least in theory, length dependent and thus could account for the length dependence of IFT recruitment that we have observed.

Assumptions.

i) We assume that the concentration gradient of RanGTP between the flagellum and the cytoplasm regulates recruitment of IFT particles to distal appendage fibers of the basal body [proposed to be the flagellar equivalent of the nuclear pore by Deane et al. (25)]. Under this assumption, the accumulation of IFT proteins at the flagellar base is equivalent to the transient accumulation of nuclear cargos at the nuclear pore that have been revealed by photobleaching and single-molecule studies (26, 27).

ii) RanGTP is produced at a constant rate within the flagellum, due to a constant activity of RanGEF (e.g., a constant number of RanGEF molecules) and a saturating amount of RanGDP that is independent of flagellar length. Because we assume that RanGDP is present in excess, it can be considered a constant and we do not directly model it.

iii) The gradient of RanGTP across the flagellar pore reaches steady state at a timescale that is fast relative to the timescale over which flagellar length changes.

iv) The flagellar compartment is well mixed, such that no spatial gradient exists within it. Assumptions *iii* and *iv* together allow us to use steady-state assumptions for the flagellar concentration of RanGTP at any given length.

v) RanGTP hydrolyzes to RanGDP at a constant rate according to first-order kinetics, with no effect of length on the hydrolysis rate.

vi) The concentration of RanGTP in the cytoplasm is always very small compared with the flagellar concentration.

vii) RanGTP escapes the flagellar compartment according to Fick's first law, $J = -D\frac{\partial \phi}{\partial x}$, where J is the diffusive flux, ϕ is the concentration, and x is pore length. We assume that $\frac{\partial \phi}{\partial x}$ is approximately equal to the flagellar RanGTP concentration divided by the pore length on the basis of assumption *vi* that the cytoplasmic RanGTP concentration is negligible. The total rate of diffusive loss of RanGTP from the flagellum is the flux, J, times the cross-sectional area, a.

viii) The flagellum is cylindrical, so volume is equal to length, L, times the cross-sectional area.

With these assumptions in mind, we describe the rate of change in the number of molecules of RanGTP within the flagellum as

$$\frac{dN}{dt} = k_{prod} - k_{cat}N - \frac{k_{esc}N}{L}, \qquad \textbf{[S1]}$$

where N is the total number of molecules of RanGTP inside the flagellar compartment, k_{prod} is the rate at which new RanGTP is produced per unit time, k_{cat} is the hydrolysis rate for RanGTP to RanGDP (inverse of the half life), L is the length of the flagellum, and k_{esc} is a proportionality constant that takes into account the diffusion constant and the length of the flagellar pore ($k_{esc} = D/l$, where D is the diffusion constant and l is the pore length).

The key point of this equation is that any given RanGTP that is produced can undergo only one of two mutually exclusive fates: either it makes it to the pore and leaks out or it undergoes nucleotide hydrolysis (Fig. 4).

We solve Eq. **S1** for the steady-state solution to obtain

$$N^* = \frac{k_{prod}}{k_{cat} + \frac{k_{esc}}{L}} \qquad \textbf{[S2]}$$

or

$$N^* = \frac{k_{prod}L}{k_{cat}L + k_{esc}}. \qquad \textbf{[S3]}$$

Examination of this equation shows that the number of RanGTP molecules reaches a limit as the length increases. However, the concentration of RanGTP in the flagellar compartment, and thus the flux out of the compartment, is proportional to $\frac{N^*}{L}$, and thus we see that the concentration decreases as the flagellar compartment grows in size:

$$[RanGTP] = \frac{k_{prod}}{k_{cat}L + k_{esc}}. \qquad \textbf{[S4]}$$

We thus conclude that the concentration of RanGTP at the flagellar pore is inherently length dependent, and if the concentration of RanGTP controls the level of IFT recruitment as proposed by Dishinger et al., then IFT recruitment and injection should be inherently length dependent. The origin of this length dependence is fundamentally very simple: The probability that a molecule of RanGTP reaches the pore before it hydrolyzes becomes smaller as the flagellum becomes longer. Because RanGTP itself in the cytoplasm could inhibit Importin-mediated accumulation of IFT material at the flagellar pore, we suggest that the length dependence of such a signal would have to be mediated through another protein, such as one of the known flagellar length mutants. However, a recent study suggests that the effect could be direct (28).

All of the parameters in the model either have been published or can be estimated. Therefore, we examined how the model behaves with published parameter values (29, 30) to determine whether the behavior is realistic (Fig. 4). We estimate the pore length to be 0.2 μm on the basis of electron microscopy data. We also varied the parameters within the published ranges to determine which parameters the model is most sensitive to (Fig. S12).

As noted, increasing the production rate increases the concentration of RanGTP at any given length, whereas increasing either the decay rate or the diffusion constant decreases the RanGTP concentration. The effects of increased diffusion rate are most pronounced at low lengths.

Finally, we note that this general model for organelle size sensing by diffusion of a metastable reporter molecule could be extended to any organelle that forms a closed compartment.

1. Mueller J, Perrone CA, Bower R, Cole DG, Porter ME (2005) The FLA3 KAP subunit is required for localization of kinesin-2 to the site of flagellar assembly and processive anterograde intraflagellar transport. *Mol Biol Cell* 16(3):1341–1354.

2. Lechtreck K-F, et al. (2009) The Chlamydomonas reinhardtii BBSome is an IFT cargo required for export of specific signaling proteins from flagella. *J Cell Biol* 187(7): 1117–1132.

3. Feldman JL, Marshall WF (2009) ASQ2 encodes a TBCC-like protein required for mother-daughter centriole linkage and mitotic spindle orientation. *Curr Biol* 19(14):1238–1243.
4. Tokunaga M, Imamoto N, Sakata-Sogawa K (2008) Highly inclined thin illumination enables clear single-molecule imaging in cells. *Nat Methods* 5(2):159–161.
5. Ludington W, Marshall W (2009) Automated analysis of intracellular motion using kymographs in 1, 2, and 3 dimensions. *Proc SPIE* 7184:71840Y–71840Y-9.
6. Engel BD, Ludington WB, Marshall WF (2009) Intraflagellar transport particle size scales inversely with flagellar length: Revisiting the balance-point length control model. *J Cell Biol* 187(1):81–89.
7. Gardner MK, Odde DJ, Bloom K (2007) Hypothesis testing via integrated computer modeling and digital fluorescence microscopy. *Methods* 41(2):232–237.
8. Magleby KL, Pallotta BS (1983) Burst kinetics of single calcium-activated potassium channels in cultured rat muscle. *J Physiol* 344:605–623.
9. Ahdesmaki M, Lahdesmaki H, Yli-Harja O (2007) Robust Fisher's test for periodicity detection in noisy biological time series. *Genomic Signal Processing and Statistics, 2007. GENSIPS 2007. IEEE International Workshop on* (Tuusula, Finland), pp 1–4.
10. Hurst HE (1957) A suggested statistical model of some time series which occur in nature. *Nature* 180:494 (lett).
11. Mandelbrot BB, Wallis JR (1969) Global dependence in geophysical records. *Water Resour Res* 5(2):321–340.
12. Politzer PA (2000) Observation of avalanchelike phenomena in a magnetically confined plasma. *Phys Rev Lett* 84(6):1192–1195.
13. Mier J, Garcia L, Sanchez R (2006) Study of the interaction between diffusive and avalanche-like transport in near-critical dissipative-trapped-electron-mode turbulence. *Phys Plasmas* 13(102308):1–10.
14. Ruzmaikin A, Feynman J, Robinson P (1994) Long-term persistence of solar activity. *Sol Phys* 149:395–403.
15. Varotsos C, Kirk-Davidoff D (2006) Long-memory processes in ozone and temperature variations at the region 60°S-60°N. *Atmos Chem Phys* 6:4093–4100.
16. Suki B, et al. (2003) Fluctuations, noise and scaling in the cardio-pulmonary system. *Fluctuation Noise Lett* 3:R1–R25.
17. Serletis A, Rosenberg A (2007) The Hurst exponent in energy futures prices. *Physica A: Stat Mech Appl* 380:325–332.
18. Willinger W, Taqqu M, Teverovsky V (1999) Stock market prices and long-range dependence. *Finance Stoch* 3(1):1–13.
19. Lillo F, Farmer J (2004) The long memory of the efficient market. *Stud Nonlinear Dyn E* 8(3):1–19.
20. Linkenkaer-Hansen K, Nikouline VV, Palva JM, Ilmoniemi RJ (2001) Long-range temporal correlations and scaling behavior in human brain oscillations. *J Neurosci* 21(4):1370–1377.
21. Chowdhury D, Schadschneider A, Nishinari K (2005) Physics of transport and traffic phenomena in biology: From molecular motors and cells to organisms. *Phys Life Rev* 2:318–352.
22. Burridge R, Knopoff L (1967) Model and theoretical seismicity. *Bull Seismol Soc Am* 57(3):341–371.
23. Huang J, Turcotte D (1990) Evidence for chaotic fault interactions in the seismicity of the San Andreas fault and Nankai trough. *Nature* 348:234–236.
24. Dishinger JF, et al. (2010) Ciliary entry of the kinesin-2 motor KIF17 is regulated by importin-beta2 and RanGTP. *Nat Cell Biol* 12(7):703–710.
25. Deane JA, Cole DG, Seeley ES, Diener DR, Rosenbaum JL (2001) Localization of intraflagellar transport protein IFT52 identifies basal body transitional fibers as the docking site for IFT particles. *Curr Biol* 11(20):1586–1590.
26. Kubitscheck U, et al. (2005) Nuclear transport of single molecules: Dwell times at the nuclear pore complex. *J Cell Biol* 168(2):233–243.
27. Lowe AR, et al. (2010) Selectivity mechanism of the nuclear pore complex characterized by single cargo tracking. *Nature* 467(7315):600–603.
28. Fan S, et al. (2011) Induction of Ran GTP drives ciliogenesis. *Mol Biol Cell* 22(23):4539–4548.
29. Klebe C, Prinz H, Wittinghofer A, Goody RS (1995) The kinetic mechanism of Ran—nucleotide exchange catalyzed by RCC1. *Biochemistry* 34(39):12543–12552.
30. Becskei A, Mattaj IW (2003) The strategy for coupling the RanGTP gradient to nuclear protein export. *Proc Natl Acad Sci USA* 100(4):1717–1722.

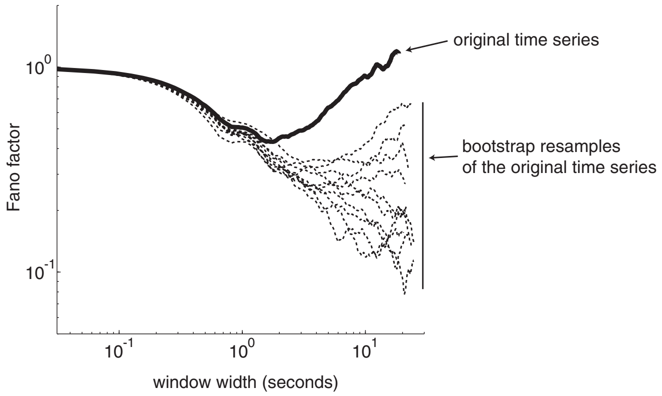

Fig. S1. Analysis of bursting in IFT. The Fano factor (i.e., variance in event number divided by mean event number) for a sample injection series (thick solid line) shows an initial decrease with increasing window size, followed by an increase in longer time windows. For each time series ($n = 40$, KAP-GFP, fla3$^-$ strain time series), time series data were converted to an event series and the number of events occurring within a sliding window was calculated. The ratio of the variance in number of events per window to the average number of events was used to calculate the Fano factor. Ten bootstrap resamples of the actual injection series (shaded dashed lines) were compared with the actual series (thick solid line). An example case is shown. Because a Poisson process has variance equal to the mean, deviation of the Fano factor from 1 indicates that the injections do not occur as a Poisson process, showing that sequential events in the injection series are not independent, such that the occurrence of one event influences the timing of the next event. This analysis is based on methods used to analyze neuronal spike trains; see, for example, ref. 1. Decreasing Fano factor with increasing window size indicates that the events are occurring with more regularity than predicted for a Poisson process and are consistent with the presence of a distinct peak in the distribution of interevent times (Fig. S9). Increase in Fano factor for largest-size windows is consistent with bursting.

1. Rieker F, Warland D, de Ruyter van Steveninck R, Bialek W (1997) *Spikes: Exploring the Neural Code* (MIT Press, Cambridge, MA).

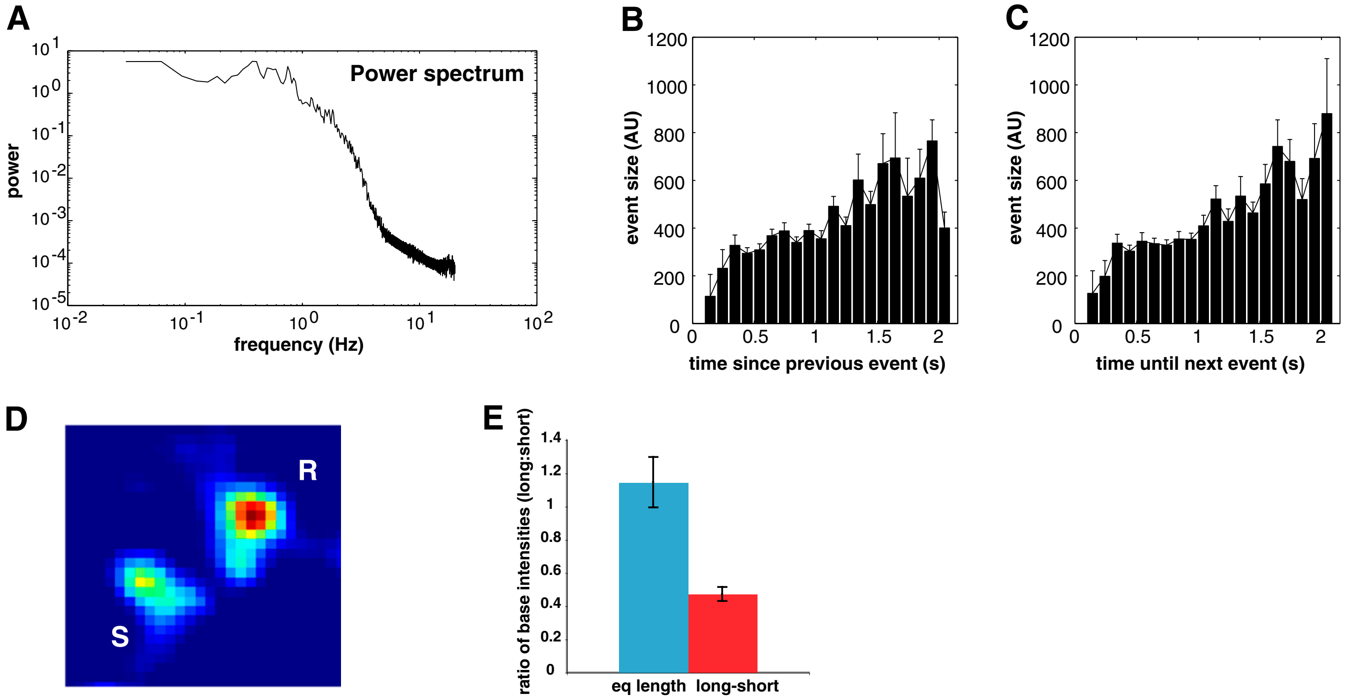

Fig. S2. IFT20-GFP rescue of ΔIFT20 shows the same injection behavior as GFP-tagged kinesin II. (*A*) The power spectrum was calculated by methods used in Fig. 1*C*. The behavior is similar to behavior seen in the kinesin II time series although false positive traces increase the apparent frequency. (*B*) The event magnitude increases with longer time interval since the previous event ($r = 0.24$; $P = 0$; $n = 1{,}367$ events). (*C*) The event magnitude is also correlated with the time interval until the next event ($r = 0.25$; $P = 0$; $n = 1{,}297$). (*D*) IFT20 accumulates in greater quantities at the base of regenerating flagella ("R") than at the base of steady-state length flagella ("S"). Intensity is represented from highest (dark red) to lowest (dark blue). (*E*) Quantified intensity ratio of S:R for five cells with unequal-length flagella and eight cells with equal-length flagella. Error bars show SEM.

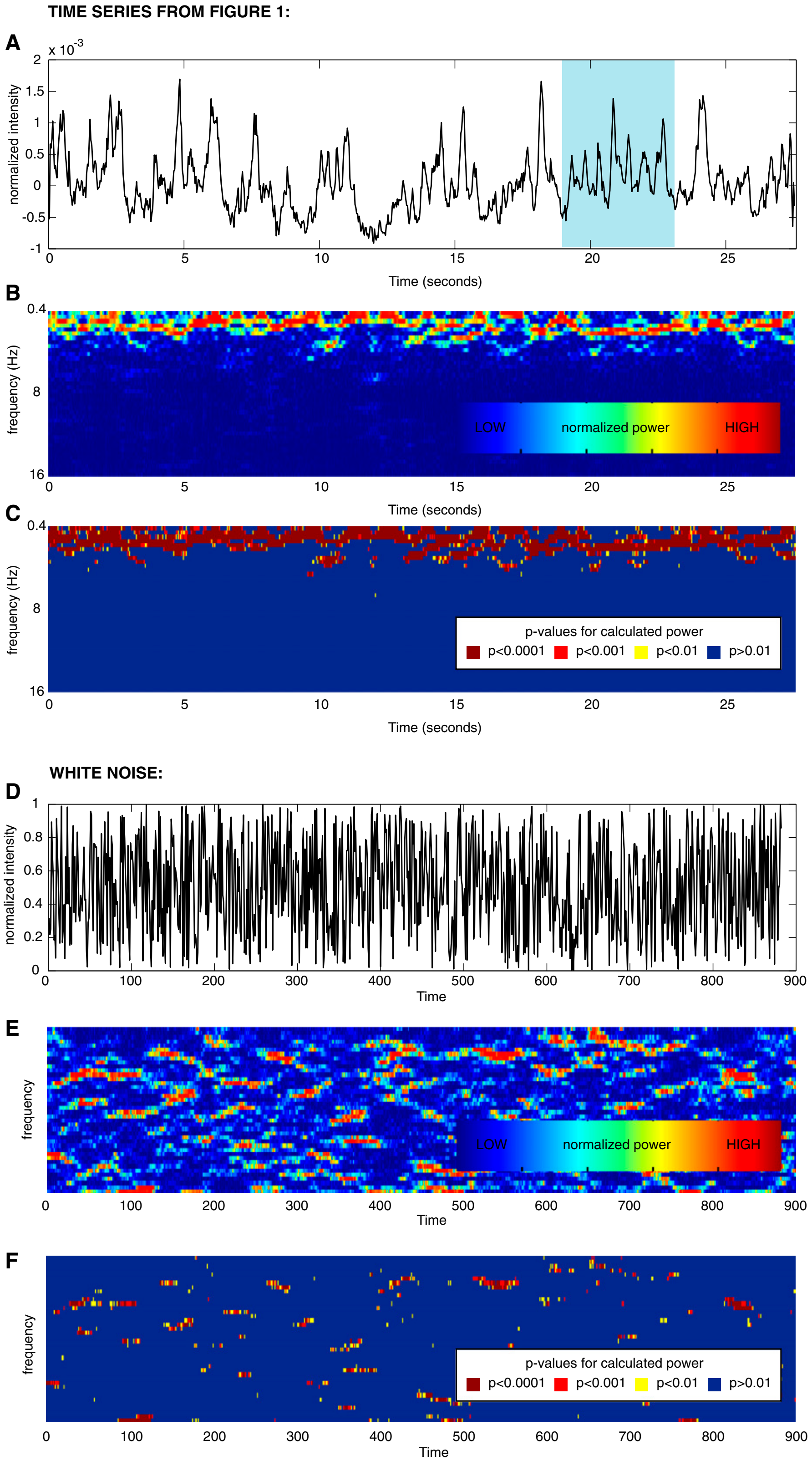

Fig. S3. Periodicity is transient. (*A*) The raw, photobleaching-corrected time series analyzed in Fig. 1 (KAP-GFP, fla3$^-$ strain). Note the visibly apparent periodic window from $\sim$19 to 23 s (shaded in blue). (*B*) The power spectrum was calculated on a rolling 2-s window for the time series shown. The *x* axis is time in the time series. The *y* axis is frequency (linear scale). Color indicates the power at each frequency band with blue being the lowest and red being the highest. Again, note the consistent periodicity at $\sim$1–2 Hz for the window from 19 to 23 s. (*C*) We used a robust version of Fisher's *G*-test (1) to calculate significant periodicities on the 2-s window along the time series. The specific algorithm that we used was named "robust" by its authors (1) because they were able to show that it is less sensitive to outliers than the standard Fisher's *G*-test. Note that every time series analyzed ($n = 218$) had significant periodicity at 1 Hz for at least 71.5% of

Legend continued on following page

the time but that the dominant frequency drifts over the course of the time series. (*D*) For contrast, we compare these results with uniform white noise. (*E*) By the same analysis, the white noise time series shows short windows of periodicity, but no drift around a dominant frequency. Instead, short spurts of periodic behavior randomly occur but are not correlated with one another. (*F*) Because we examine the series on a rolling window, periodic events in one window tend to be observed over multiple adjacent windows, producing significant periodicities at the same frequency for several adjacent windows.

1. Ahdesmaki M, Lahdesmaki H, Yli-Harja O (2007) Robust Fisher's test for periodicity detection in noisy biological time series. *Genomic Signal Processing and Statistics, 2007. GENSIPS 2007. IEEE International Workshop on* (Tuusula, Finland), pp 1–4.

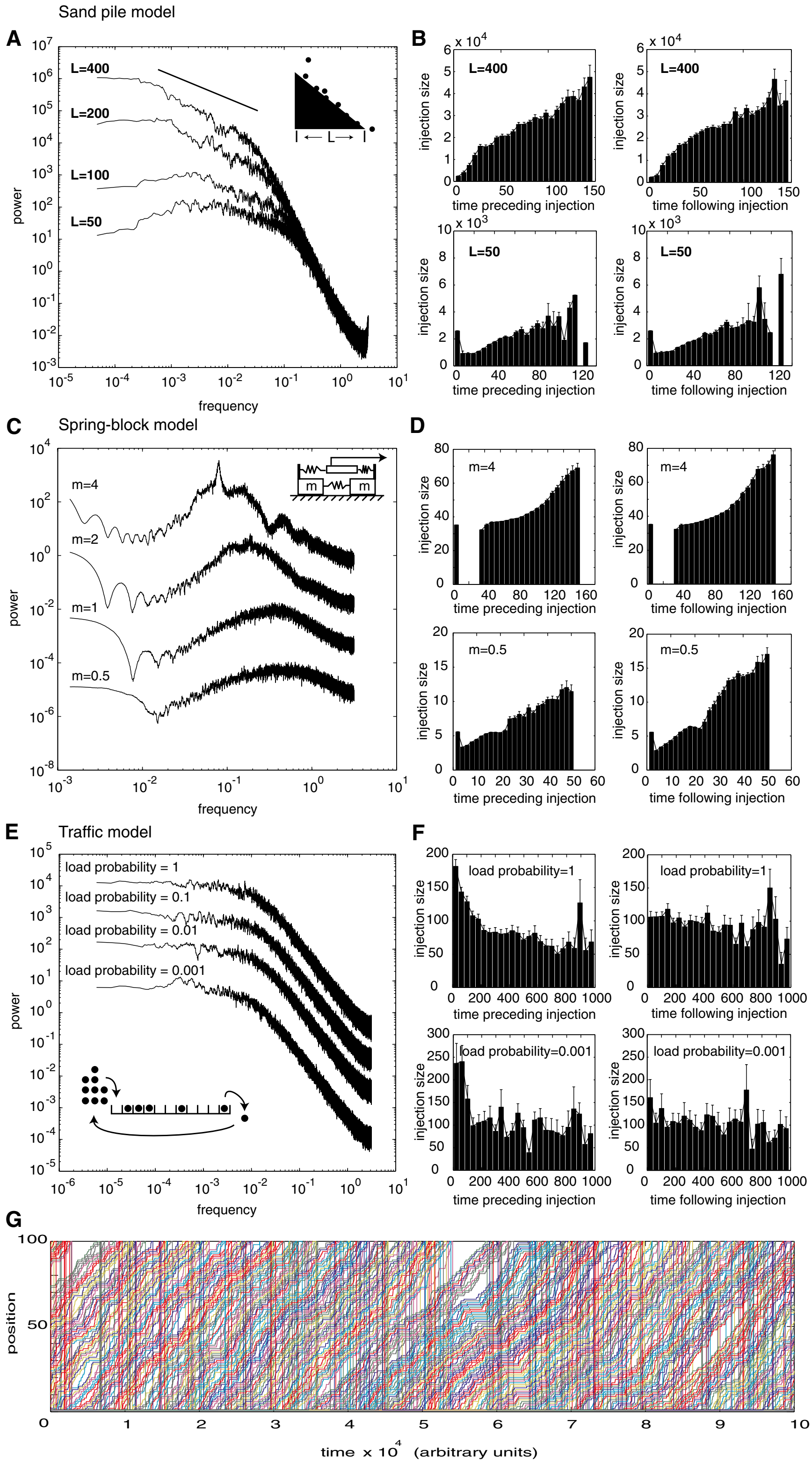

Fig. S4. Comparison of avalanche and traffic-jam models that reproduce relaxation oscillators. Computational models that allow storage of potential energy show better concordance with the data when we vary the system parameters. (*A*) In the sandpile avalanche model (1), the power spectrum of energy dissipation, E_t, the number of sand grain movements in a time step, shows some periodicity at low pile width (*L*, *Inset*) and begins to show 1/f noise in a limited frequency range (10^{-3}–10^{-1} Hz) due to overlapping avalanches for large system sizes (solid line above the power spectra indicates slope 1/f) (1). We used the exact equations and parameters used by Hwa and Kardar (1) with *L* varied as indicated. Power spectra are not offset. For reader reference, the height of sand in the system, *H*, at a given position, *n*, at time, *t*, updates at each time step according to the equations

$$H(n, t+1) = H(n, t) - N_f$$
$$H(n \pm 1, t+1) = H(n \pm 1, t) + N_f$$

Legend continued on following page

if and only if

$$H(n,t) - H(n \pm 1,t) > \Delta.$$

Our simulations used $N_f = 2$ and $\Delta = 8$. One sand grain is added to a randomly chosen position every 10 time steps rather than waiting for the system to equilibrate before adding another grain. Readers should refer to Hwa and Kardar (1) for a very clear explanation of the model, parameter choices, and implications. We waited until the model became stationary before recording the output. (*B*) Event magnitudes for the sandpile model correlate with both the time interval preceding a release and the time interval following release for both large and small pile widths. (*C*) A simplified version of the Burridge–Knopoff spring-block model (1, 2) (diagram) shows a broad peak, resembling experimental measures of sandpile data (3), and is similar to the kinesin II and IFT20 datasets for small masses. However, the system becomes highly periodic when larger masses (*m*, *Inset*) are used. Power spectra are calculated for the movement of the forward block and are offset on the power axis so that they can be distinguished. The block positions, X_1 and X_2, at time *t*, update according to the equations

$$X_i(t+1) = X_i(t) + \frac{F_{top\_spring} + F_{side\_spring}}{F_{friction}},$$

where

$$F_{spring} = -k_{spring}\Delta x$$

$$F_{friction} = k_{friction} m \frac{rand - 0.5}{8}$$

$$k_{friction} = \begin{cases} k_{sliding} & moving \\ k_{static} & stationary. \end{cases}$$

We use friction proportional to mass because we assume a constant density; thus more massive blocks are longer and have more frictional contacts. The number of frictional contacts is proportional to the block length with up to one-eighth of the friction determined randomly from a uniform distribution. For the simulations shown, $k_{sliding} = 2$, $k_{static} = 2.1$, and $k_{spring} = 0.005$, and the overhead block is driven at 0.5 distance units per time step. *m*, the mass of the sliding blocks, was varied as indicated. (*D*) Event magnitudes for the sliding-block model correlate with both the time intervals preceding and those following events regardless of system size. Larger masses have both longer time intervals and larger-magnitude events. (*E*) A traffic-jam model (4) (see *Inset* diagram but note that the track length is 500 bins in the actual computational implementation of this model) shows white noise at low frequency and power law decay ($\alpha = -1.78$) at higher frequencies regardless of the motor density on the track. Although there is some qualitative concordance with the injection data, the real data show white noise, some periodicity, and a roll off (nonpower law), whereas the traffic model is dominated by the power law decay. Power spectra were offset so that they can be distinguished. To represent movement of motors along the track, the position, *P*, of the *i*th motor at time *t* updates according to the equation $P(i,t+1) = P(i,t) + 1$ if the motor is on the track with a free space in front of it. If the space in front is blocked by another motor, then the position of the motor does not change. Update of motor positions is asynchronous with motors being selected at random and updated individually. If the selected motor at time *t* is at the final track position, it is removed from the track and recycled to the pool of motors awaiting entry onto the track. If the selected motor is in the pool of motors awaiting entry onto the track, then the position of the motor is set to 1 with a fixed probability set by the parameter load_probability. The power spectrum was taken for the flow, *J*, of motors exiting the track per unit time, recorded after this flow had become stationary. (*F*) The traffic model shows a slight negative correlation between the time interval preceding an event and the event size. Event size does not correlate with the time intervals following events. These trends, which are clearly divergent from the trends seen in the sandpile model (Fig. S4*B*) and in experimental IFT data (Fig. S6*B*), hold regardless of the motor density on the track. All simulations were recorded for 1,000,000 time steps. Irrelevant, low-frequency regions of the power spectra were cropped out. (*G*) Typical kymograph of traffic model shows formation of jams. Each color trace represents one motor as it travels across the track and is recycled to position zero. Jams occur when motors impede each other's movement due to motor density on the track and are indicated by horizontal stretches of the traces for several motors occurring in parallel.

1. Hwa T, Kardar M (1992) Avalanches, hydrodynamics, and discharge events in models of sandpiles. *Phys Rev A* 45(10):7002–7023.
2. Huang J, Turcotte D (1990) Evidence for chaotic fault interactions in the seismicity of the San Andreas fault and Nankai trough. *Nature* 348:234–236.
3. Jaeger HM, Liu Ch, Nagel SR (1989) Relaxation at the angle of repose. *Phys Rev Lett* 62(1):40–43.
4. Chowdhury D, Schadschneider A, Nishinari K (2005) Physics of transport and traffic phenomena in biology: From molecular motors and cells to organisms. *Phys Life Rev* 2:318–352.

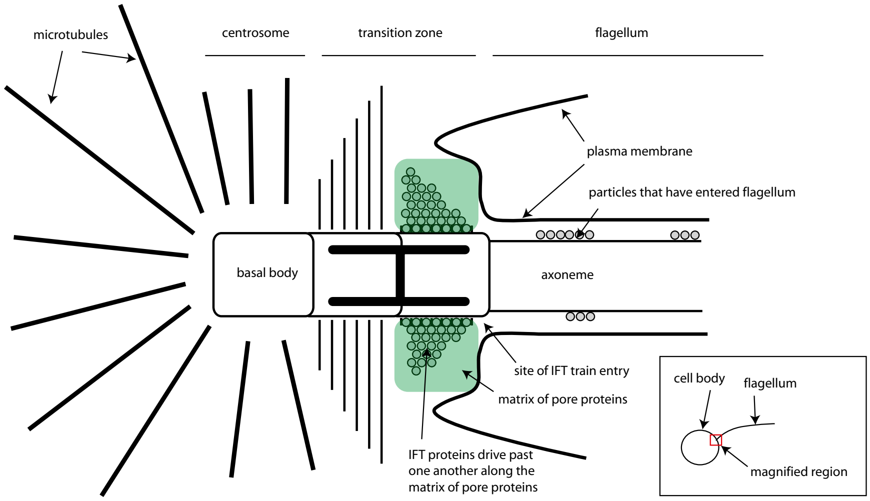

Fig. S5. Diagrammatic model of the known components of the flagellar IFT train injection apparatus. Intraflagellar transport trains localize to the basal body and accumulate at the flagellar pore, at the distal end of the basal body. The IFT trains drive past one another in the transition fibers and matrix proteins, which additionally filter out proteins that are not licensed for entry. A computational model based on this diagram is presented in Fig. S6 *C* and *D*.

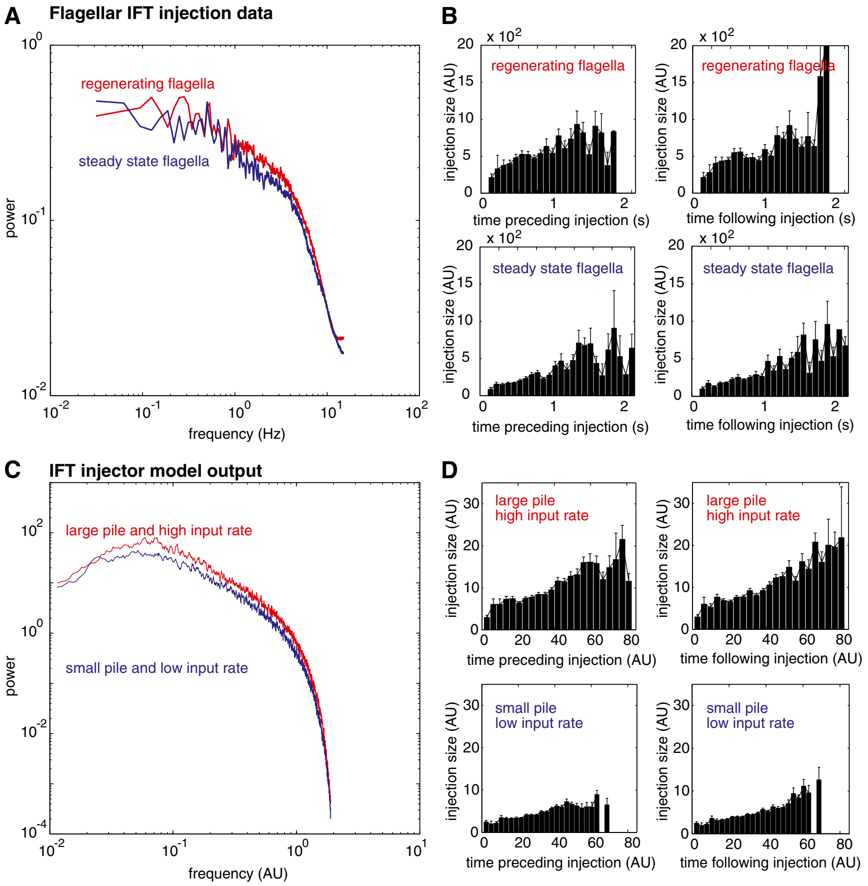

Fig. S6. Computational model of the IFT injector shows concordance with the empirical data. Time series data from KAP-GFP fla3$^-$ strain cultures undergoing flagellar regeneration were sorted according to flagellar length (regenerating <7 μm, $n = 24$, mean = 5.2 μm, SEM = 0.15 μm vs. steady state >12 μm, $n = 41$, mean = 13.3 μm, SEM = 0.18 μm). (*A*) Power spectra were calculated by first correcting the time series for photobleaching and then making the time series stationary (i.e., subtracting the mean). The mean squared amplitude at each frequency was then calculated using standard Fourier-based methods in MATLAB. These power spectra differ slightly from the one presented in Fig. 1*C* because local detrending was used in Fig. 1*C*, whereas, for consistency with Hwa and Kardar (1), it was not used in calculating the power spectrum in Fig. S4 *A*, *C*, and *E* nor was it used in the power spectra presented here. A minimum time series length of 8 s was used and time series longer than 8 s were cropped to 8 s. We note that at higher frequencies, smoothing of data and the shape of the injection peaks start to influence the power spectrum, potentially explaining differences between model and data at frequencies greater than 1 Hz. (*B*) Local detrending was used to calculate injection sizes and time intervals between injections here, in Fig. 2 *A* and *B* and in Fig. S4 *B*, *D*, and *F*. Hwa and Kardar (1) noted the difficulty in computationally distinguishing overlapping avalanches, and we apply the strategy of local detrending because it allows us to compare trends in individual events with the previous work done on IFT injections (2, 3). (*C*) Model of avalanching in the IFT injection system. Whereas the sandpile model in Fig. S4 *A* and *B* showed clear similarities to the experimentally obtained behavior, it was not obvious how the elements of that model related to actual components of the IFT system. To directly model the known components of the IFT injection system, we built a computational model of IFT injections, as diagrammed in Fig. S5. We model the movements of IFT particles through the transition zone of the basal body as follows: We represent the IFT docking sites on the distal region of the basal body by an annular lattice with nine parallel arrays of binding sites and a fixed length L_B (set to 7 in our simulation based on approximate lengths of IFT trains and the length of the transition zone by electron microscopy), with the number of IFT particles at each lattice site given by an integer $T(i, j, t)$, where $1 \leq i \leq 9$ and $1 \leq j \leq L_B$. The lattice of binding sites has a lateral periodic boundary condition, a closed (proximal) end, and an open (distal) end. Bound particles move in a directed fashion from the basal body into the flagellum driven by molecular motor forces, which are opposed by the presence of other particles blocking their path. IFT train movement occurs when any of the following conditions are met:

$$T(i,j,t) - T(i,j+1,t) > k$$

$$|T(i,j,t) - T(i+1,j,t)| > k.$$

These conditions indicate that IFT trains can shift position in either a distal-directed or a lateral direction, but cannot move in a proximal direction due to the directionality of kinesin motors. Here k is a constant reflecting the ability of bound IFT particles to impede the movement of additional IFT particles into a given binding region. When any of these conditions are met, a constant number N_m move into the grid space, either distal or lateral, with the array T updated accordingly. Movements occur laterally and distally but not proximally. New IFT particles bind the flagellar base in random positions on the lattice at a rate of B (L) particles per time step, where L is the flagellar length (Fig. 4*D*). We note that in our simulation, we do not model flagellar length dynamics and so B is a constant that we can increase or decrease to represent changes in basal body accumulation rates for short vs. long flagella. IFT particles docked on the flagellar base enter the flagellum by exiting the transition zone area, which is represented as an additional row of lattice points at the distal end; i.e., $j = L_B + 1$. Any IFT particles entering this last row of lattice points are then removed from the simulation at each time step and summed to yield the flux of injected material flowing into the flagellum at that time step:

$$J_o(t) = \sum_{i=1}^{9} T(i, L_B + 1, t)).$$

For the simulation results presented, we used the parameter values

Legend continued on following page

$$k = 8$$
$$N_m = 2$$

and $B = 3$ for full-length flagella (blue curve) and $B = 5$ for short regenerating flagella (red curve). (*C*) The power spectrum of this flux for two simulations of 1 million time steps each. The blue curve shows a simulation with three trains added per time step, and the red curve shows a system with five trains added per time step, corresponding to the fold difference in flux measured empirically in the IFT system between full-length and short flagella. The general trends of the power spectra match what we measured (*A*). (*D*) The relationships between event magnitudes and interarrival times for the simulations in *C*. These simulation results show the same qualitative trends as the data presented in *B*, including a larger average injection size for regenerating flagella compared with steady-state flagella. In addition, the Hurst exponent for the model prediction was calculated to be 0.7, which is comparable to the experimentally measured value of 0.6. The ratio of total particles in the small grid vs. the large grid was 0.69 at the end of the simulation, which agrees with our experimental data from Fig. 4*B*.

1. Hwa T, Kardar M (1992) Avalanches, hydrodynamics, and discharge events in models of sandpiles. *Phys Rev A* 45(10):7002–7023.
2. Engel BD, Ludington WB, Marshall WF (2009) Intraflagellar transport particle size scales inversely with flagellar length: Revisiting the balance-point length control model. *J Cell Biol* 187(1):81–89.
3. Dentler W (2005) Intraflagellar transport (IFT) during assembly and disassembly of Chlamydomonas flagella. *J Cell Biol* 170(4):649–659.

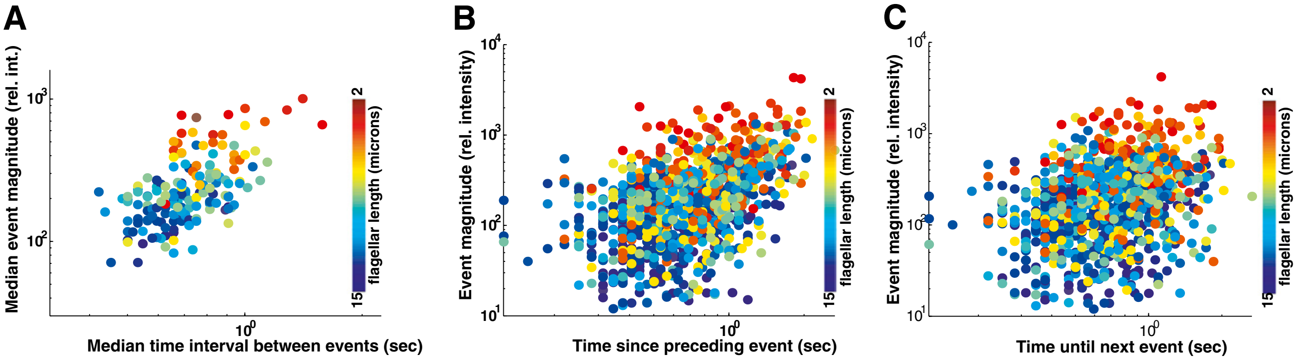

Fig. S7. Injection behavior is length dependent. (*A*) The median injection event size and median time interval between injection events were calculated for 168 flagella (KAP-GFP, fla3⁻ strain). Longer flagella tend to make smaller injections, and they tend to make injections more frequently. Likewise, shorter flagella tend to make larger injections, and they tend to make injections less frequently. Note the correlation between injection size and injection time interval. Even though short flagella tend to have large median injection sizes, when a short flagellum (red circles) has a smaller median injection size, it also has a shorter median time interval between injections. And to the same point, whereas longer flagella (blue circles) tend to have smaller injections, when a long flagellum does have large injections, these injections occur less frequently (i.e., with a longer median time interval between injections). (*B*) The median trends of event magnitude and the timing of events are also apparent when observing individual injection events. Longer time intervals preceding an injection tend to lead to larger injections. (*C*) The same is true for the time intervals following an injection: Larger injections tend to be followed by a longer time before the next injection occurs, although this trend is less strong than for the time interval preceding the injection. All of the data presented are for time series where burst integration was not performed (*SI Materials and Methods*). The effects of burst integration are minor. Flagellar lengths are color coded with blue for long and red for short (see color scale).

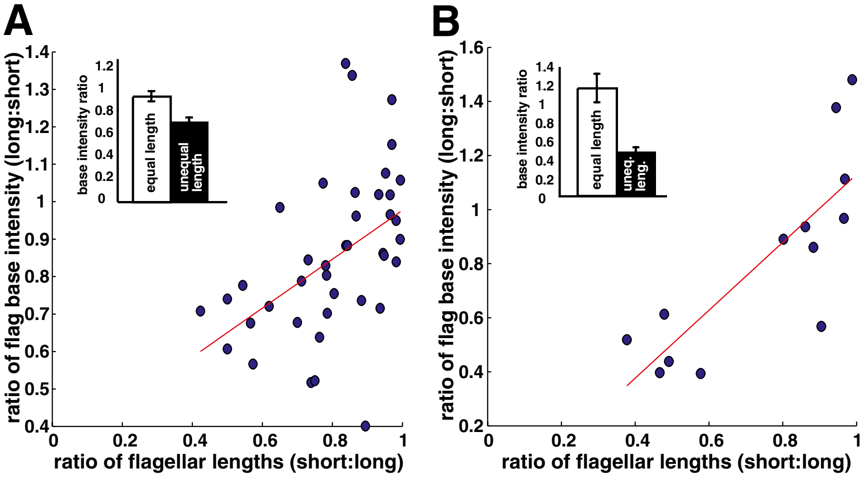

Fig. S8. More IFT material accumulates at the base of faster-growing flagella. (*A*) The accumulated load of kinesin-II (KAP-GFP, fla3⁻ strain; KAP-GFP fluorescence) is greater at the base of the shorter flagellum in single cells with unequal-length flagella. (*Inset*) The difference in accumulation where groups have been divided on the basis of a length ratio of 0.8. (*B*) The accumulated load of IFT20 (IFT20-GFP, ΔIFT20 strain; IFT20-GFP fluorescence) is greater at the base of the shorter flagellum in single cells with unequal-length flagella. (*Inset*) The difference in accumulation where groups have been divided on the basis of a length ratio of 0.8. Red lines are robust linear fits from MATLAB.

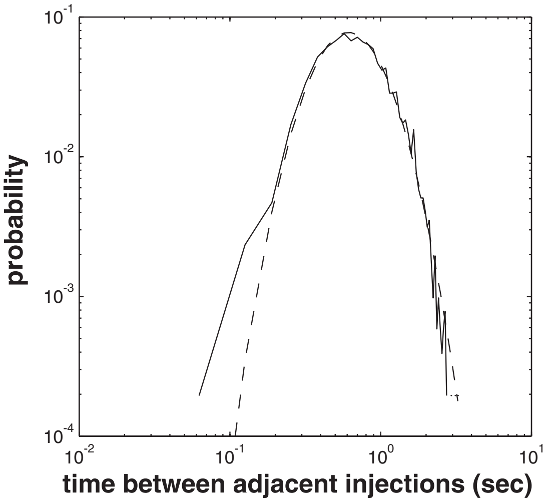

Fig. S9. Distributions of interarrival intervals for non–burst-integrated injection events (KAP-GFP, fla3⁻ strain). The distribution of time intervals between adjacent injections (solid line) fits well with a lognormal distribution (dashed line). It is a much narrower distribution than the injection magnitude distribution (Fig. 1*D*), which is dominated by its tail, whereas the intervals distribution is dominated by its center.

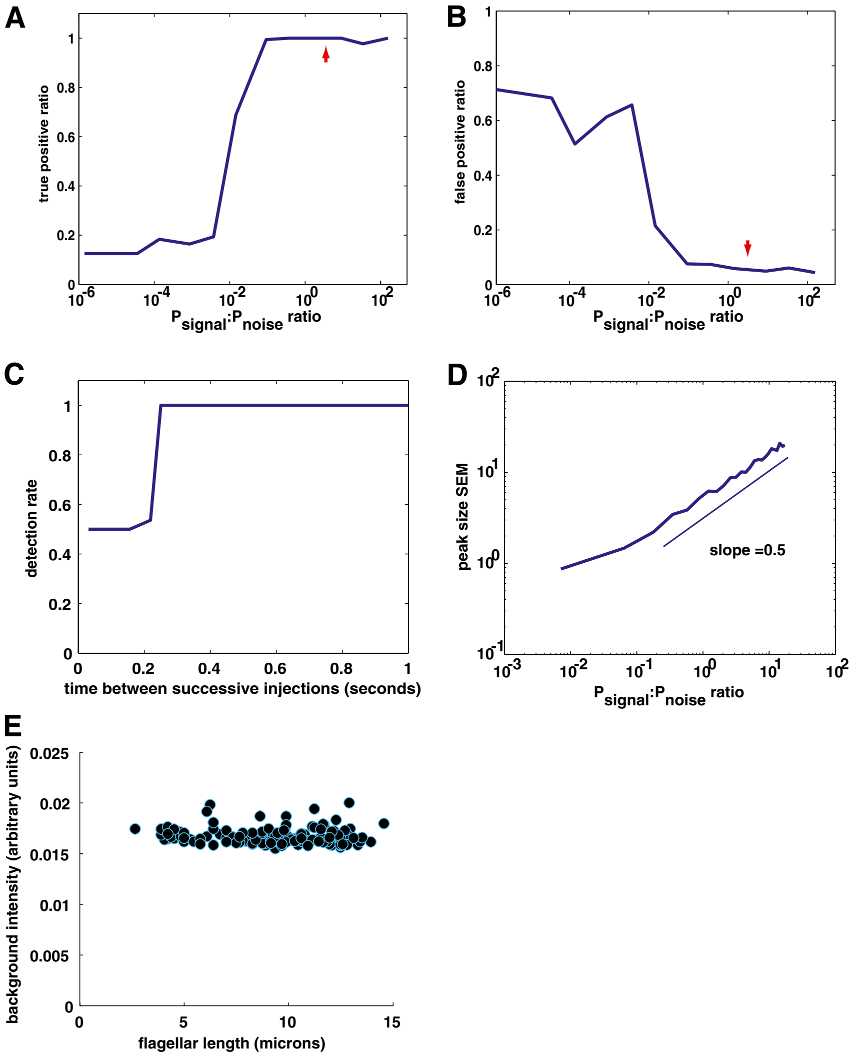

Fig. S10. Kymograph processing algorithm performance evaluated using model convolution. (*A* and *B*) We made synthetic kymographs, varying the signal-to-noise ratio from 1.4×10^{-6} to 156, and then evaluated the ratio of (*A*) true positive and (*B*) false positive calls, as a function of the signal-to-noise ratio. The algorithm functions well above a signal-to-noise ratio of 0.1. We estimate the actual signal-to-noise ratio to be 2.5 (red arrows). On the basis of these performance tests, we should see 5% false positives and 100% true positives. We calculate the false positive ratio as the number of wrong calls divided by the total number of calls. The true positive ratio is the number of correct calls divided by the number of possible correct calls. (*C*) To evaluate the time resolution, we evaluated the algorithm performance over varying input frequencies to determine how close together injections can be before they are merged into a single event by the algorithm. Synthetic kymographs were made with doublet injections 1 s apart. The spacing between the peaks in a doublet was varied from 0.03 s to 1 s. The algorithm performs well for intervals 0.25 s and above, whereas shorter intervals cause the adjacent injections to be merged into a single event. (*D*) We also calculated the SE in estimating injection size as a function of the signal-to-noise ratio. As injections get larger, the error in estimating their absolute size increases as the signal-to-noise ratio to the 1/2 power. (*E*) The background intensity (KAP-GFP, *fla3*$^{-}$ strain) is roughly constant as a function of flagellar length ($r = -0.09$, $P > 0.24$, $n = 168$ flagella).

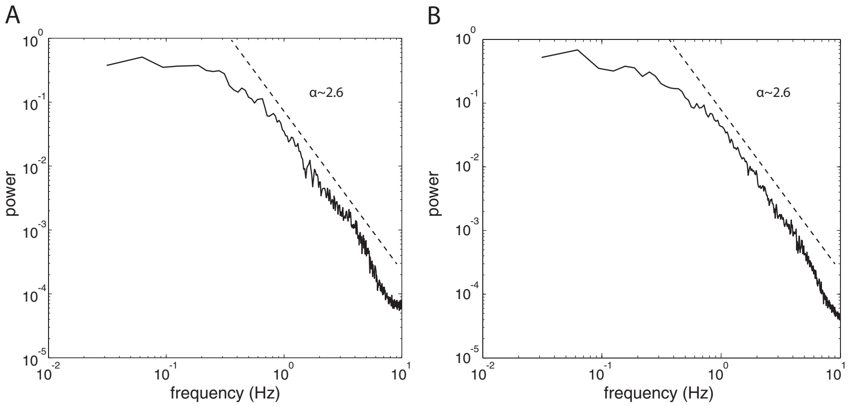

Fig. S11. Power spectra of raw time series show power law behavior. (*A* and *B*) We calculated the power spectra for raw time series of KAP-GFP injections (*A*) and IFT20-GFP injections (*B*). The power spectra appear to have roughly power law behavior with a slope of $\alpha \sim 2.6$.

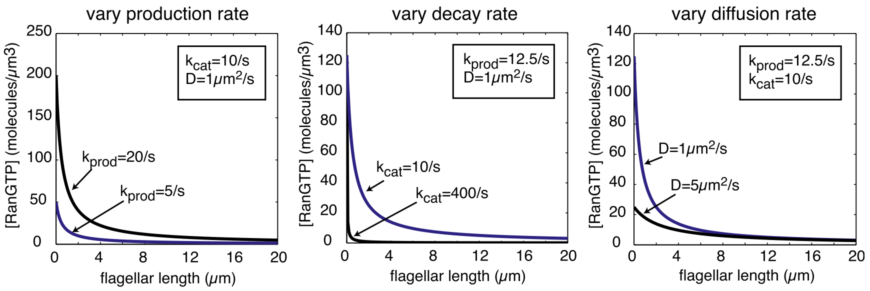

Fig. S12. Sensitivity of RanGTP gradient model for length sensitivity to variation of model parameters. The model in *SI Appendix* was used to predict variation of RanGTP concentration at the flagellar pore as parameters describing production, degradation, and diffusion of RanGTP were varied over a range based on estimated parameters from existing literature.

Table S1. Several alternative biochemical models do not explain our results

Model	Hypothesis	Data in support	Data against
a) Entry-gated pore	Pore opens when more material is needed (frequency-modulated control).	—	*i*) The injection rate is uncorrelated with the amount of time that material is entering the flagellum.
b) Checkpoint	Larger trains take longer to enter because more cargo must be checked.	*i*) Injection magnitude is correlated with the length of the time interval preceding the injection.	*i*) Injection magnitude is correlated with the length of the time interval following the injection. *ii*) Bursting is not explained. *iii*) Periodicity is not explained.
c) Constant accumulation rate and random release timing	Material accumulates at the entry point at a constant rate. The gate opens at random time intervals and lets all of the accumulated material in.	*i*) Injection magnitude is correlated with the length of the time interval preceding the injection.	*i*) Injection magnitude is correlated with the length of the time interval following the injection. *ii*) Bursting is not explained. *iii*) Periodicity is not explained. *iv*) A standing load of material is present at the flagellar base.
d) Biochemical clock	A biochemical oscillator at the base controls entry timing.	*i*) Periodicity.	*i*) Bursting. *ii*) The frequency changes as the injection rate changes. *iii*) Larger accumulation gives slower dynamics. *iv*) No explanation for the regulation of IFT train size.

Dishinger et al. (24) presented evidence that several biochemical regulators of the nuclear import system are at work in the mammalian cilium. Thus, a potential model for the injector is that of (*a*) a regulated entry channel, with open and close times set by a flagellar length-dependent control system (i.e., the channel opens more often when the flagellum needs more material). This model predicts a strong positive correlation between the injection rate and the percentage of time where IFT trains are flowing through the pore. In fact, we observe an insignificant negative correlation ($r = -0.12$, $P = 0.09$, $n = 218$ flagella). Another nuclear import-type model is (*b*) a checkpoint crossing model, where larger trains take a longer time to transit the pore because each subunit in the IFT train takes a finite time to transit the pore. So, longer trains take longer to enter. That type of model correctly predicts the correlation between the injection size and the time interval preceding an injection (Figs. 2*A* and 3*C* and Figs. S2*B* and S7*B*). However, such a model does not account for the bursting behavior (Fig. S1), the correlation between injection size, and the time interval following an injection (Fig. 2*B* and Figs. S2*C* and S7*C*) or the periodicity that we observe (Fig. 1*C* and Figs. S3 and S6*A*). The same is true for a trivial model in which (*c*) IFT material accumulates at a constant rate and then releases into the flagellum at random times. Such a mechanism could explain the correlation between injection size and preceding time interval but cannot explain the bursting, periodicity, or correlation between injection size and the following time interval. (*d*) Biochemical clocks, such as those from circadian systems, are composed of a set of nonexchanging proteins that keep time in a consistent manner even in lack of a driving force (e.g., night–day cycling). The analog for the IFT system would be an injector that allows IFT train entry based on its cycling biochemical state. Our data indicate that a throughput of material (i.e., exchanging components) regulates injection timing and that the timing is not consistent, e.g., the bursting dynamics (Fig. S1) and the lognormal distribution of time intervals between injections (Fig. S9).